Earth Planet. Sci. Lett. 638 (2024) 118757

Contents lists available at ScienceDirect

Earth and Planetary Science Letters

journal homepage: www.elsevier.com/locate/epsl

Assessing lunar paleointensity variability during the 3.9 - 3.5 Ga high field epoch

Ji-In Jung [a,*], Sonia M. Tikoo [a,b], Dale Burns [b], Zoltán Váci [c], Michael J. Krawczynski [c]

[a] Department of Geophysics, Stanford University, Stanford 94305, CA, USA
[b] Department of Earth and Planetary Sciences, Stanford University, Stanford 94305, CA, USA
[c] Department of Earth, Environmental, and Planetary Sciences, Washington University in St. Louis, St. Louis 63130, MO, USA

ARTICLE INFO

Keywords:
Lunar paleomagnetism
Paleointensity reliability
Intermittent dynamo
Lunar magnetic carriers

ABSTRACT

Numerous paleomagnetic studies suggest that a lunar dynamo, with surface field intensities potentially as high as 40-100 μT, existed between ~3.9 Ga and ~3.5 Ga. This period is referred to as the High Field Epoch (HFE). However, the debate over the origin of magnetization recorded in lunar rocks still persists. In addition, whether the Moon could have sustained a continuously strong dynamo during the HFE remains unclear. To unravel the origin of magnetization preserved in lunar rocks and to better characterize the evolution of the ancient lunar dynamo, we conducted a comprehensive set of experiments including rock magnetic tests, electron microscopy, and paleomagnetic investigations on four HFE-aged Apollo 11 mare basalt samples: 10003, 10044, 10069, and 10071. Rock magnetic experiments and electron microscopy indicate that the remanence carriers are kamacite grains of varying sizes and domain states. Sample 10003 recorded a paleointensity of 54.10 ± 4.66 μT. Sample 10044, which was shocked (peak pressure >5 GPa), did not preserve a stable high coercivity remanent magnetization. Samples 10069 and 10071 recorded paleointensities of 61.46 ± 26.09 μT and 10.69 ± 2.87 μT, respectively. A series of hydrostatic pressure experiments, isothermal remanent magnetization (IRM) acquisition experiments, and viscous remanent magnetization (VRM) tests preclude the possibility of our samples containing shock remanent magnetization from transient impact-generated fields, IRM acquisition from exposure to spacecraft fields, and VRM acquisition from exposure to the Earth magnetic field. Overall, our study suggests that the source of these magnetizations was likely the lunar dynamo and may indicate nearly order-of-magnitude magnetic field fluctuations during the HFE.

1. Introduction

Decades of investigations into lunar crustal magnetism and paleomagnetism have collectively indicated that the Moon generated an ancient dynamo field [Weiss and Tikoo, 2014; Tikoo and Evans, 2022; Wieczoreck et al., 2023]. Lunar crustal magnetism dominantly provides insight into the Moon's early magnetic history (> 3.8 Ga) [Hood, 2011; Hood et al., 2021]. Magnetic anomalies within the central melt sheets of several Pre-Nectarian, Nectarian, and Imbrian impact basins are interpreted to record magnetization acquired from a relatively stable surface magnetic field (such as that produced from a dynamo) [Hood and Spudis 2016; Hood et al., 2021; Halekas et al. 2003; Oliveira et al. 2017]. This is because the massive central melt sheets of impact basins are expected to cool far more slowly (>10,000 years) than the short (<1 day) duration of transient impact plasma fields [Hood 2011]. Recent paleomagnetic studies of Apollo samples suggest that the lunar field initiated by 4.25 Ga [Garrick-Bethell et al., 2017] and later produced at least intermittently high surface fields with intensities ranging from 40 to 110 μT [Cournède et al., 2012; Shea et al., 2012; Suavet et al., 2013; Weiss and Tikoo, 2014; Nichols et al., 2021] (Fig. 1). This period, known as the high field epoch (HFE), persisted from ~3.9 until ~3.5 Ga and was succeeded by a decline in the surface magnetic field to below 10 μT after 3.5 Ga [Tikoo et al., 2014; Tikoo et al., 2017; Strauss et al., 2021]. It is unclear if the dynamo continuously or intermittently operated after 3.5 Ga, but the lack of remanence in young lunar impactites indicates that the field likely ceased sometime between 1.9 and 0.8 Ga [Tikoo et al., 2017; Mighani et al., 2020].

A mystery persists regarding how the Moon could have produced intense fields during the HFE. This is primarily because the Moon's core is too small and would have cooled too rapidly to produce continuously

* Corresponding author.
E-mail address: jiinjung@stanford.edu (J.-I. Jung).

https://doi.org/10.1016/j.epsl.2024.118757
Received 13 September 2023; Received in revised form 2 May 2024; Accepted 4 May 2024
Available online 14 May 2024

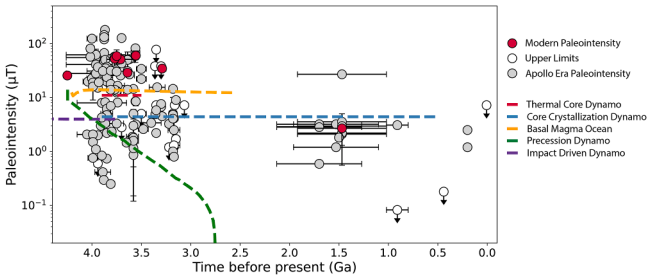

Fig. 1. Paleointensity determinations of Apollo samples (circles) and estimated surface fields from theoretical lunar dynamo models (dashed lines) versus radiometric age. Paleointensities and associated uncertainties are shown in logarithmic scale. Red, white, and grey circles represent paleointensity estimates from recent studies, upper limits, and Apollo-era datasets, respectively [Garrick-Bethell et al., 2009; 2017; Cournède et al., 2012; Shea et al., 2012; Suavet et al., 2013; Tikoo et al., 2012, 2014, 2017; Mighani et al., 2020; Nichols et al., 2021; Strauss et al., 2021; Tarduno et al., 2021]. Red, blue, yellow, green, and purple dashed lines represent estimated dynamo surface fields powered by thermal core convection [Evans et al., 2018], core crystallization [Evans et al., 2018], basal magma ocean [Schienberg et al., 2018], impacts [Le bars et al., 2011], precession [Dwyers et al., 2011], respectively. Note that paleointensity values were recalculated using new mean calibration factors (see main text for details) [Wieczoreck et al., 2023]. Multiple data points for the Apollo-era dataset may correspond to the same sample but in such cases, each point was obtained by using different methods or in different studies.

high (>10 μT) surface fields for an extended period via conventional thermochemical convection dynamo power sources, including gravitational, differential, latent, and radiogenic heat energy [Evans et al., 2018]. As such, unconventional dynamo mechanisms have been suggested, including a basal magma ocean dynamo [Scheinberg et al., 2018; Hamid et al., 2023], an impact-driven dynamo [Le Bars, 2011], and either mechanical or thermal dynamos driven by precession [Dwyer et al., 2011; Cébron et al., 2019; Stys and Dumberry, 2020]. However, none of these models can produce continuously strong surface fields throughout the HFE (Fig. 1).

While numerous studies have inferred >10 μT paleofields during the HFE [Cournède et al., 2012; Shea et al., 2012; Suavet et al., 2013; Weiss and Tikoo, 2014; Nichols et al., 2021], other recent studies have claimed the possibility of low or null fields during the same period [Cournède et al., 2012; Tarduno et al., 2021; Lawrence et al., 2008; Lepaulard et al., 2019] (Fig. 1). In particular, Lepaulard et al., [2019] inferred substantial variations in magnetic intensity during the HFE based on a paleointensity proxy derived from the ratio of natural remanent magnetization (NRM) to magnetic susceptibility. However, issues with this method include the absence of magnetic cleaning and the associated inability to conclusively decipher the nature and origin of the NRM in samples. Intriguingly, Apollo-era measurements also hint at large paleointensity variability up to two orders of magnitude during the HFE [Fuller and Ciswoski, 1987; Cisowski et al., 1983]. Because numerous recent paleomagnetic studies specifically targeted high paleointensity samples identified from the Apollo-era dataset (1970 – the 1980s), it is possible that those studies overlooked samples with low or null paleointensities. However, we also note that many Apollo-era paleointensity estimates should be re-evaluated due to advances in methodology over time.

Two explanations might reconcile the mismatch between theoretical lunar dynamo models and the actual paleointensity results. First, the variability observed in the collective paleointensity record could stem from the intrinsic behavior of the lunar dynamo caused by factors such as magnetic reversals and excursions that are commonly observed in the paleointensity record of Earth [Selkin and Tauxe, 2000]. It has also been proposed that the Moon may have generated an episodically intense dynamo [Evans et al., 2018]. Le Bars et al. [2011] introduced the concept of a dynamo driven by basin-forming impact events that could persist for several thousand years post-impact. However, this mechanism produces a field strength that is an order of magnitude lower than the observed HFE paleointensities. More recently, Evans and Tikoo [2022] proposed that the sinking of cold, dense titanium-rich diapirs to the core-mantle boundary could stimulate strong, intermittent dynamo activity during the HFE [Evans and Tikoo, 2022].

Second, lunar paleointensities may be affected by non-dynamo processes such as remagnetization by shock pressures [Gattacceca et al., 2010b] in the presence of transient impact-generated fields [Tarduno et al., 2021; Crawford, 2020], acquisition of isothermal remanent magnetization (IRM) generated by spacecraft fields [Tikoo and Jung, 2023], or viscous remanent magnetization (VRM) after exposure to the geomagnetic field [Dunlop, 1973; Weiss and Tikoo, 2014]. Uncertainties may also arise from samples' poor magnetic recording properties [Tikoo et al., 2012] or methodological issues. Methodological issues may include studies using nonideal paleointensity methods (e.g., thermal methods that may lead to sample alteration versus non-thermal methods that may have an intrinsic factor ~2-5 uncertainty) [Suavet et al., 2014; Wieczorek et al., 2023], or different studies implementing varying paleointensity acceptability criteria [Selkin and Tauxe, 2000; Lawrence et al., 2008; Tikoo et al., 2012].

In this study, we investigated four HFE-aged Apollo 11 mare basalts, two of which have never previously been subjected to paleomagnetic studies. We performed electron microscopy and rock magnetic experiments to identify the dominant magnetic carriers in the samples. We also conducted a comprehensive paleomagnetic study employing non-heating paleointensity methods, as well as a series of experiments to account for the origin of magnetization. Finally, we discuss the aforementioned possible origins of magnetization for our samples and assess lunar paleointensity variability during the HFE.

2. Sample Descriptions and Magnetic Carriers

2.1. Sample Descriptions

In this work, we studied mare basalts 10003, 10044, 10069, and 10071. All of these samples have different cosmogenic exposure ages, indicating that they were likely excavated to the lunar surface at different times [Turner, 1970; Guggisberg et al., 1979]. Samples 10003 (crystallization age ~3.91 ± 0.03 Ga) and 10044 (~3.73 ± 0.05 Ga) are relatively old low-K basalts, and samples 10069 (~3.54 ± 0.01 Ga) and 10071(~3.51 ± 0.06 Ga) are young high-K ilmenite basalts [Stöffler et al., 2006; Stettler et al., 1974; Turner, 1970]. Two of these samples (10003, 10069) were previously reported in the Apollo-era literature to have relatively low paleointensity values (< 5 μT) [Cisowski et al., 1983; Helsey, 1970]. The other two samples (e.g., 10044, 10071) were previously unstudied. Our optical microscopy analysis revealed no significant petrological evidence of shock (indicating peak pressures < 5 GPa; a shock degree of S1 [Fritz et al., 2017; Stoffler et al., 2006; 2018]) for all samples, with the exception of sample 10044. Sample 10044 displayed undulatory extinction in pyroxene grains, indicating that this sample experienced pressures >5 GPa. All samples were sliced into four mutually oriented subsamples (~80 - 300 mg each) using a diamond wire saw for paleomagnetic investigations and rock magnetic experiments. All sample numbers for thin sections and bulk samples, as well as lithologic descriptions, radiometric ages, and Apollo-era paleointensity values are tabulated in Table 1.

2.2. Magnetic Mineral Characterization

2.2.1. Methods

We employed both electron microscopy and rock magnetic experiments to characterize the dominant magnetic carriers in our samples. In order to determine the petrological and compositional relationships between crystalline phases within our sample set, one thin section from each sample was imaged using a JEOL JSM-IT500HR field-emission scanning electron microscope equipped with a backscatter electron

Table 1
Lunar HFE mare basalt samples used in this study and prior paleomagnetic and geochronology results.

Thin Section	Bulk Sample	Lithology	Age (Ga)	Exposure Age (My)	Apollo-era PI (μT)
10003, 184	10003, 217	Low-K Ilmenite basalt	3.91 ± 0.03 [1]	137 [2]	4.33 [5]
10044, 49	10044, 673	Low-K Cristobalite basalt	3.73 ± 0.05 [2]	80	None
10069, 33	10069, 99	High-K Ilmenite basalt	3.54 ± 0.01 [3]	40 [4]	2.29 [5], 1.51 [6]
10071, 31	10071, 127	High-K Ilmenite basalt	3.51 ± 0.06 [1]	370 [4]	None

The first and second columns detail the thin section and rock samples used in our study, respectively. The third column contains the lithology. The fourth and fifth columns contain 40Ar/30Ar radiogenic age and 37Ar/38Ar cosmic ray exposure ages, respectively. The sixth column contains Apollo-era paleointensities reported for these samples. References:[1] Stettler et al., 1974; [2] Turner, 1970; [3] Stöffler et al, 2006; [4] Guggisberg et al. 1979; [5] Cisowski et al., 1983 [6] Helsley, 1970.

detector at the Stanford Microchemical Analysis Facility. After this initial characterization, quantitative compositional analyses of the distinct phases were completed using JEOL JXA-8230 Electron Probe Micro-analyzer (EPMA). The EPMA is equipped with five wavelength dispersive spectrometers including one large-format spectrometer optimized for minor and trace element measurements A detailed description of EPMA run conditions and methods are presented in Section S2. We also investigated the detailed structures of 3-15 μm diameter FeNi grains in all four samples (1 grain for 10003 and 10069; and 2 grains for 10044 and 10071) using transmission electron microscopy (TEM). Sample preparation by Focused Ion Beam (FIB) extraction and all TEM analyses including high-angle annular dark field (HAADF) and bright-field (BF) imaging were conducted at the Institute of Material Science and Engineering (IMSE) at Washington University in Saint Louis using a STEM Thermo Fisher Scios 2 DualBeam FIB and JEOL JEM-2100F Field-Emission STEM, respectively.

To better understand magnetic mineralogies, grain sizes, and domain states, one subsample from each rock was subjected to magnetic hysteresis, backfield remanence [Section S3.1], and first-order reversal curve (FORC) measurements [Section S3.2] using a Lake Shore Vibrating Sample Magnetometer (VSM) at the Institute for Rock Magnetism at the University of Minnesota. In addition, we performed an isothermal remanent magnetization (IRM) acquisition experiment and unmixing of coercivity spectra using the MaxUnmix software [Robertson and France, 1994; Maxbauer et al., 2016] [Section S3.3]. IRM experiments were conducted using a 2G Enterprises 755 superconducting rock magnetometer (sensitivity limit $\sim 10^{-12}$ Am^2) equipped with automated rock magnetic characterization instrumentation that is housed within a magnetically shielded room (ambient field <200 nT) at Stanford Paleomagnetism Laboratory. IRM was applied along the z-axis in these experiments.

2.2.2. Results

Initial electron microprobe analyses and magnetic hysteresis parameters suggested that the predominant remanence carriers are likely multidomain (MD) FeNi alloys, similar to mare basalts described in other recent lunar paleomagnetic studies [Shea et al., 2012; Suavet et al., 2013; Tikoo et al., 2012; Tarduno et al., 2021]. Our electron microprobe analysis indicates that most of the FeNi grains are embedded in troilite (FeS) as part of a eutectic assemblage [Fig. 2a]. Our WDS results indicate these FeNi grains are kamacite (α-Fe_{1-x} Ni_x for $x < \sim 0.05$), as elemental abundances of Ni were $\leq$2 wt. % [see Section S2]. Magnetic hysteresis [Fig. 2b], FORC analyses [Fig. 2c], and IRM unmixing results [Fig. 2d] collectively indicate the presence of low coercivity (< 100 mT) grains. However, IRM unmixing results typically revealed 3 population components in each sample: a first low coercivity component (9-36% from the extrapolated contribution [EC] calculated from the MaxUnmix software), a second medium coercivity component (45-73%), and a third high coercivity component (11-19%). The first component is consistent with MD kamacite, whereas the second and third components (with coercivities reaching >100 mT particularly for 10069 and 10071) may be indicative of SD grains.

Our FORC diagrams displayed a vertical distribution along the vertical B_u axis, also indicating a dominant population of MD grains. However, our FORC diagrams also display wide spreading along the horizontal $B_u = 0$ axis that extended to higher coercivity levels (>100 mT), indicating the presence of a single-domain (SD) grain distribution. Remanent coercivity (B_{cr}) values for samples 10069 and 10071 (84 mT and 100 mT, respectively) are higher than those typically reported for mare basalts (average value of 35 mT [Strauss et al., 2021]). For comparison B_{cr} values for 10003 and 10044 were 23 mT and 43 mT.

Our TEM HAADF and BF imaging revealed that all samples contain kamacite grains with defects and minor lattice distortions. However, kamacite grains within 10069 and 10071 contain small sub-grains (10-100 nm wide) with variable orientations that are not apparent in 10003 and 10044 [see Section S2.6; Fig.. S6]. This difference could be related to 10069 and 10071 being from a different petrologic group (Group A) than the other samples (Groups B1 and B2) [Beaty and Albee, 1980]. Because the transition from SD to MD in native iron typically occurs in the size range of 20-50 nm [Muxworthy and Williams, 2015], some of the FeNi sub-grains may be SD. This observation also aligns with IRM unmixing results that indicated a population of high coercivity (> 100 mT) grains for 10069 and 10071.

These subgrain structures do not appear to be shock related as 1) the silicate minerals in these samples do not show any shock features, likely limiting peak pressures to 5 GPa; 2) while shock can induce Neumann banding twins in kamacite at pressures of 1.5-13 GPa, we do not see this particular texture in our samples (e.g., Ohtani et al., [2022]; Luo et al., [2024]). Therefore, we suggest the observed sub-grains may either reflect primary crystallization or a decomposition feature associated with primary cooling, although the precise formation mechanism is unclear and merits further investigation. The remanence carrying properties of these sub-grains could not be fully explored as part of the current study. It is alternatively possible that an unobservable population of small isolated (i.e., not associated with troilite) high coercivity, SD FeNi grains exists. Ongoing magnetic imaging studies may address these outstanding questions.

3. Paleomagnetic Investigations

3.1. NRM behavior and paleointensity

3.1.1. Methods

Paleomagnetic analyses were conducted on three subsamples (named a, b, and c) prepared from each of our four samples. All subsamples were subjected to stepwise alternating field (AF)-demagnetization (up to 100 mT). At each step, AFs were applied along three orthogonal directions (AF along x, y and z) in a cyclic fashion using the following protocol: AFz, AFx, AFy (then measured the moment), then AFz (measured moment again), and finally AFy (measured moment again). The final magnetic moment was calculated by averaging these moments (which correspond to the final three orthogonal AF applications) to reduce the effect of gyroremanent magnetization (GRM) [Stephenson, 1980] and spurious anhysteretic remanent magnetization (ARM) [Garrick Bethell et al., 2017; Tikoo et al., 2012]. Then, each "c" subsample was subjected to room-temperature ARM paleointensity experiments (using dc bias fields of 10, 30, 40, 60, and 100 μT and an ac field of 200 mT) and saturated IRM (sIRM) paleointensity experiments (using a saturation field of 900 mT) [Weiss and Tikoo, 2014; Wieczoreck et al., 2023]. We followed modern non-heating paleointensity (i.e., ARM and sIRM) methods, described by the following expressions:

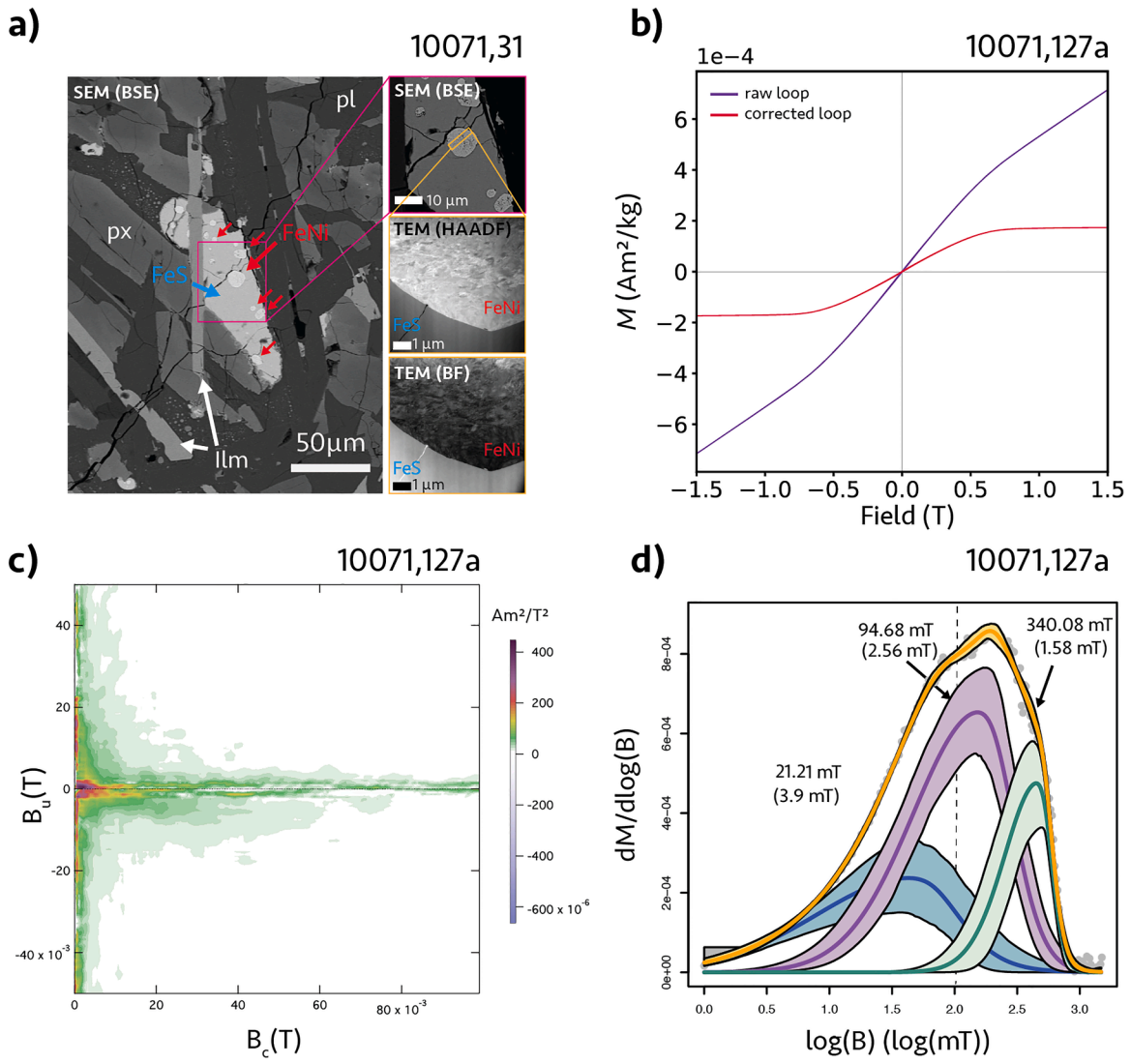

Fig. 2. Magnetic mineral characterization for the sample 10071. (a) Electron microscopy investigation of FeNi grains within FeS (troilite) for sample 10071,31. The left image is a Back Scattered Electron (BSE) image providing context for these assemblage with plagiocalse (pl), ilmenite (Ilm) and pyroxene (px). The right images include a detailed zoom on the assemblage (top) indicating the area for Focused Ion Beam (FIB) extraction (orange square) for TEM analysis, followed by High-angle annular dark-field (HAADF) (middle) and Bright-Field (BF) (bottom) images of the extracted FIB section. (b) Magnetic hysteresis curves. The purple curve shows the raw hysteresis loop, whereas the red curve shows the paramagnetic positive slope corrected loop. (c) FORC diagram for sample 10071,127a. The FORC diagram presents the density plot of the mixed second derivative of reversal curves, illustrating the degree of magnetostatic interactions (Bu) in correlation with the associated magnetic coercivity (Bc). FORC distributions were calculated by stacking 5 FORC experiments (N=268 FORC each) using the FORCinel software package [Harrison and Feinberg, 2008]. (d) The IRM unmixing results for 10003,271a derived from its backfield remanence curve using the MAX-UnMix software package [Maxbauer et al., 2016]. The actual data points and the best-fit model are illustrated by gray circles and a yellow curve, respectively. Different coercivity components and 95% confidence intervals are represented by lines and shading of different colors with the mean coercivity (numbers outside the brackets) and dispersion parameters (numbers inside the bracket). A dashed line indicates 100 mT, the maximum AF demagnetization field applied in this study.

$$B_{anc} = \frac{1}{f'}\frac{\Delta NRM}{\Delta ARM}B_{lab}$$

$$B_{anc} = a\frac{\Delta NRM}{\Delta sIRM}B_{lab}$$

where B_{anc}, B_{lab}, ΔNRM, ΔARM, and ΔsIRM are ancient magnetic field, applied laboratory field, and moment changes in NRM, ARM, and sIRM, respectively. Here, we used calibration factors of f' = 1.30 and a = 2070 μT for the ARM and sIRM methods (these are geometric means recalculated from paleointensity calibration tables in the supplementary material of Weiss and Tikoo [2014]). Because our paleointensity determinations only include AF levels < 100 mT, the predominant magnetic carriers associated with our paleointensity estimates are likely to be MD kamacite grains. All paleomagnetic experiments were conducted using 2G Enterprises 755 superconducting rock magnetometers (sensitivity limit ~10^{-12} Am^2) housed within magnetically shielded rooms (ambient fields <300 nT). AF demagnetization of NRM and sIRM paleointensity experiments were conducted in the Stanford Paleomagnetism Laboratory, whereas ARM paleointensity experiments were conducted at the MIT Paleomagnetism Laboratory.

Although non-heating paleointensity methods have long been used to avoid thermochemical alteration [Ciswoski et al., 1983; Weiss and Tikoo, 2014], concerns have been raised regarding these methods due to their reliance on poorly determined empirical calibration constants. The calibration factors f' (ARM method) and a (sIRM method) are log-normally distributed when values are compiled for many samples and are dependent on magnetic mineralogy and domain state [Weiss and Tikoo, 2014]. For lunar rocks dominated by multi-domain metallic FeNi

grains, the ARM calibration factor f' has a geometric mean of 1.3 and a geometric standard deviation (σ) of 1.18 (note this is a multiplicative factor), whereas the sIRM calibration factor has a geometric mean of 2070 μT with a geometric σ of 2.20 [Weiss and Tikoo, 2014; Wieczoreck et al., 2023]. Some paleomagnetism studies on Apollo samples have found these values to be valid, as non-heating paleointensity values are similar to those obtained via the double-heating IZZI method in a controlled atmosphere [Tikoo et al., 2017; Weiss et al., 2023]. Here, we also explored whether paleointensity variability in our samples could be due to true magnetic field behavior rather than the uncertainties associated with our paleointensity determinations. We used a Monte Carlo approach to explore whether the obtained paleointensities from our samples are truly different from each other [method details described in Section S4.3]. First, we estimate potential ranges for both paleointensity and sample age obtained by randomly selecting variables including: 1) Sample ages (within Gaussian-distributed uncertainties) obtained via geochronology studies for these samples or others from the same petrologic group. 2) Paleointensity values obtained from our study. The associated Student t-test uncertainties were based on the standard deviation calculated either from different bias fields (for ARM paleointensities) or different subsamples. 3) Paleointensity calibration factors following a log-normal distribution. We applied a permutation-based hypothesis test to determine if the paleointensity differences between two samples (10069 and 10071) are statistically distinct, given the aforementioned uncertainties. Finally, we explore whether paleointensity variability during the HFE could be due to true magnetic field behavior rather than the uncertainties associated with our paleointensity determinations.

3.1.2. Results

All subsamples have NRM values ranging from 10^{-6} – 10^{-5} Am^2/kg. These subsamples contained low coercivity (LC), medium coercivity (MC), and high coercivity (HC) magnetization components [Fig. 3]. Component directions were obtained by principal component analysis (PCA) [Kirschvink, 1980]. Both LC (0 mT to 2-8 mT, depending on the specimen) and MC (2-8 mT to 8-30 mT) components were nonuniform in direction, potentially reflecting curved magnetic field lines associated with IRM contamination during sample preparation or transit [Tikoo and Jung, 2023] or heterogeneously acquired VRM [Weiss and Tikoo, 2014]. With the exception of the shocked sample 10044,673, HC (8-30 to 100 mT) components in all samples were roughly unidirectional (α_{95} of 38.9° and κ of 11 for 10003,217; α_{95} of 29.1° and κ of 19 for 10071,

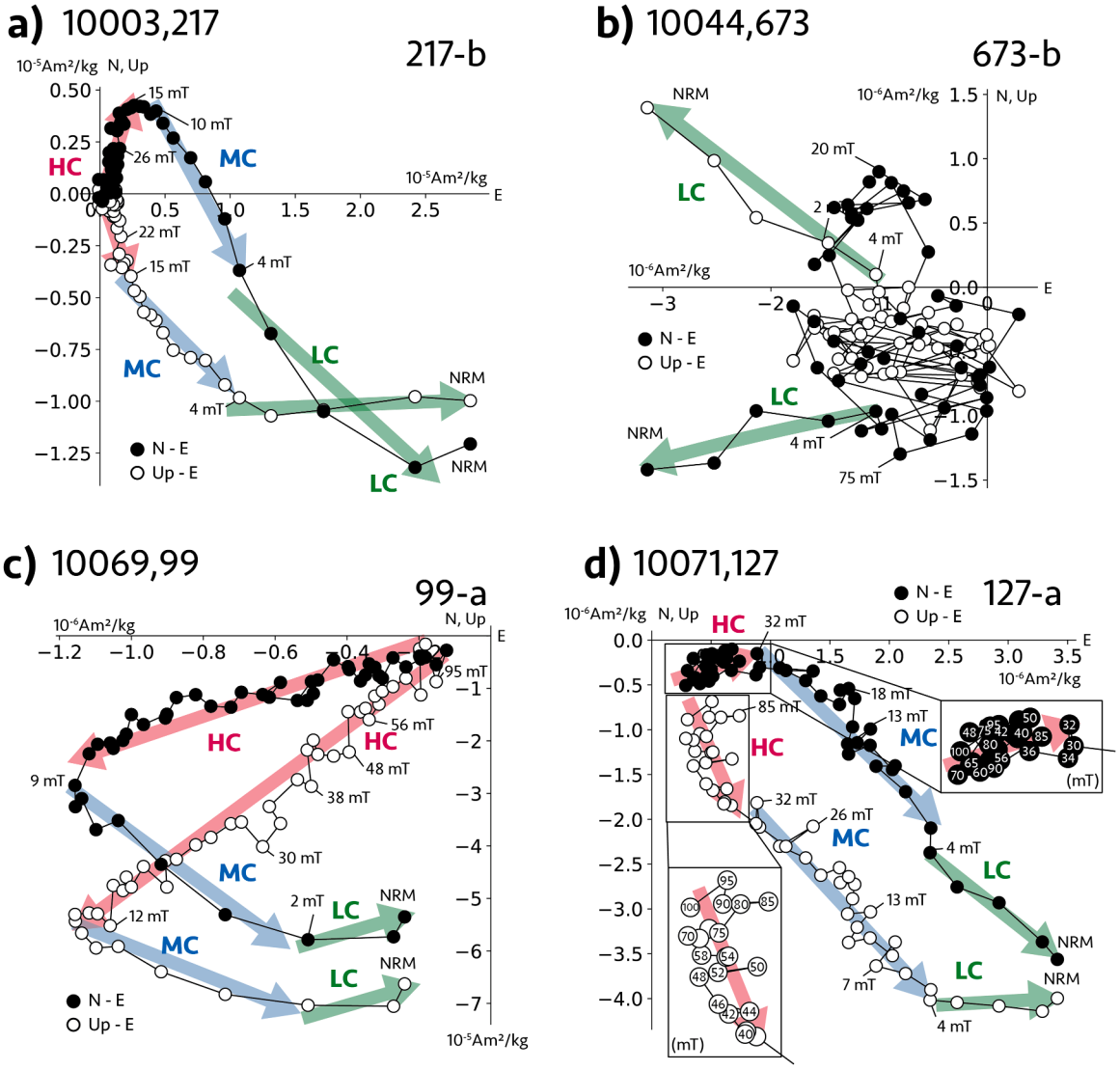

Fig. 3. Vector endpoint diagrams for subsamples (a) 10003,217b, (b) 10044,673b, (c) 10069,99a, and (d) 10071,127a. Green, blue, and red shaded arrows indicate the LC (low coercivity), MC (medium coercivity), and HC (high coercivity) components, respectively. Vector endpoint diagrams for other subsamples are shown in Fig. S11. The insets in (d) provide a detailed zoom-in view of the HC components with their associated mT vector components.

127; angular difference of 28.0° between 10069,99a and 10069,99b). We set a threshold for maximum angular deviation (MAD) of 30° for choosing subsamples for paleointensity calculations. The PCA results for 10044,673 indicate that the HC components from this sample have high MAD values ranging from 39.2 – 48.4°, suggesting they may not be ideal for reliable paleointensity retrieval. However, samples 10003,217b, 10069,99, and 10071,127 had somewhat lower MAD values of 16.9°, 4.6 – 5.9°, and 24.4 – 29°, respectively, and their deviation angles (DANG) were lower than their MAD, indicating the HC components were origin-trending for these two samples [Shea et al., 2012, Suavet et al., 2013, Lawrence et al., 2008].

Here we present average ±1 standard deviation ARM and sIRM paleointensity values calculated from the HC fractions of each sample [Fig. 4, 5; Table 2; Section S4]. Subsamples 10003,217a and c had NRM demagnetizations too unstable to obtain paleointensity values. However, for 10003,217b, we obtained a sIRM paleointensity of 54.10 ± 4.66 μT [Fig. 5a]. The NRM demagnetization data for all subsamples of 10044,673 were too unstable for paleointensity determinations [Fig. 4b; Fig. 5b]. The averaged paleointensity for sample 10069,99, which has a stable NRM, is 61.46 ± 26.09 μT (ARM paleointensity of 79.91 ± 12.69 μT [Fig. 4c] and sIRM paleointensity of 43.00 ± 8.68 μT [Fig. 5c]). These values for samples 10003 and 10069 are more than an order of magnitude higher than an Apollo-era paleointensity estimate from this rock [Cisowski et al., 1983; Helsey, 1970] but similar to other paleointensity estimates from HFE samples [Shea et al., 2012; Suavet et al., 2013; Nichols et al., 2021]. Sample 10071,127 has a relatively low paleointensity at 10.69 ± 2.87 μT (ARM paleointensity of 12.72 ± 2.88 μT [Fig. 4d] and sIRM paleointensity of 8.65 ± 3.03 μT [Fig. 5d]).

We note that the AF demagnetization to (100 mT) of our samples 10069,99 and 10071,127 qualitatively resemble that of ARM (even though the ARMs were imparted with a higher 200 mT ac field) [Fig. 6]. The NRM and ARM are both cleaned at lower AF levels than sIRM. We posit that the recording of the original NRM and our laboratory ARM was inhibited in the high coercivity (>100 mT) fraction due to magnetic interactions between Fe sub-grains. IRM would be significantly less affected by this because it is relatively concentration-independent compared to other forms of remanence such as thermoremanent magnetization (TRM) or ARM. For TRM and ARM, intensity decreases with increasing grain concentration [Sugiura, 1979]. Partly due to this effect, the coercivity spectra of TRM (or NRM) may not match that of

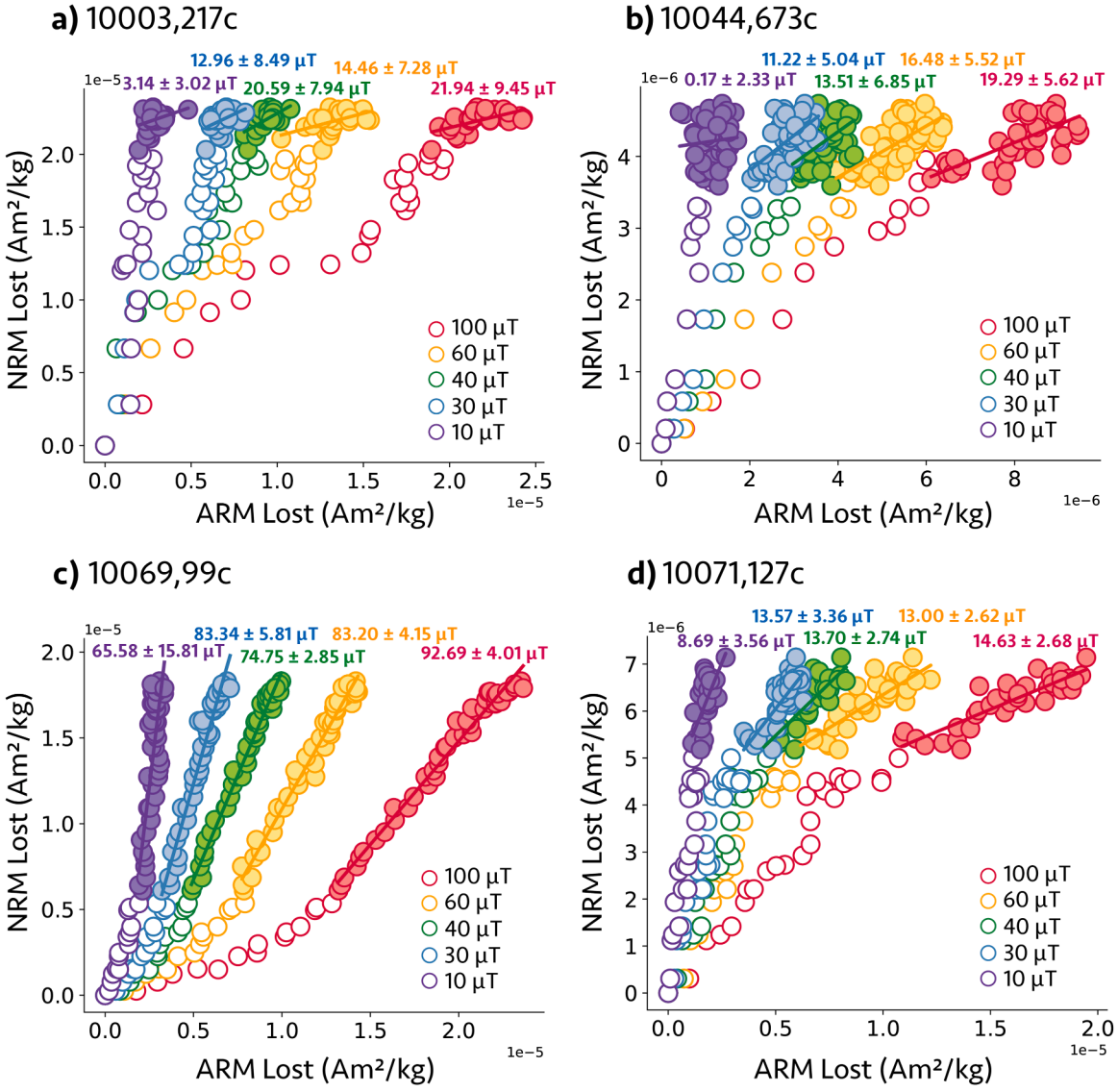

Fig. 4. ARM paleointensity results. ARM lost vs NRM lost for (a) 10003,127c, (b) 10044,673c, (c) 10069,99c, (d) 10071,127. Red, yellow, green, blue, and purple circles represent ARM acquired in dc-bias fields of 100 μT, 60 μT, 40 μT, 30 μT, and 10 μT, respectively. Filled circles denote high coercivity data points used for paleointensity estimations.

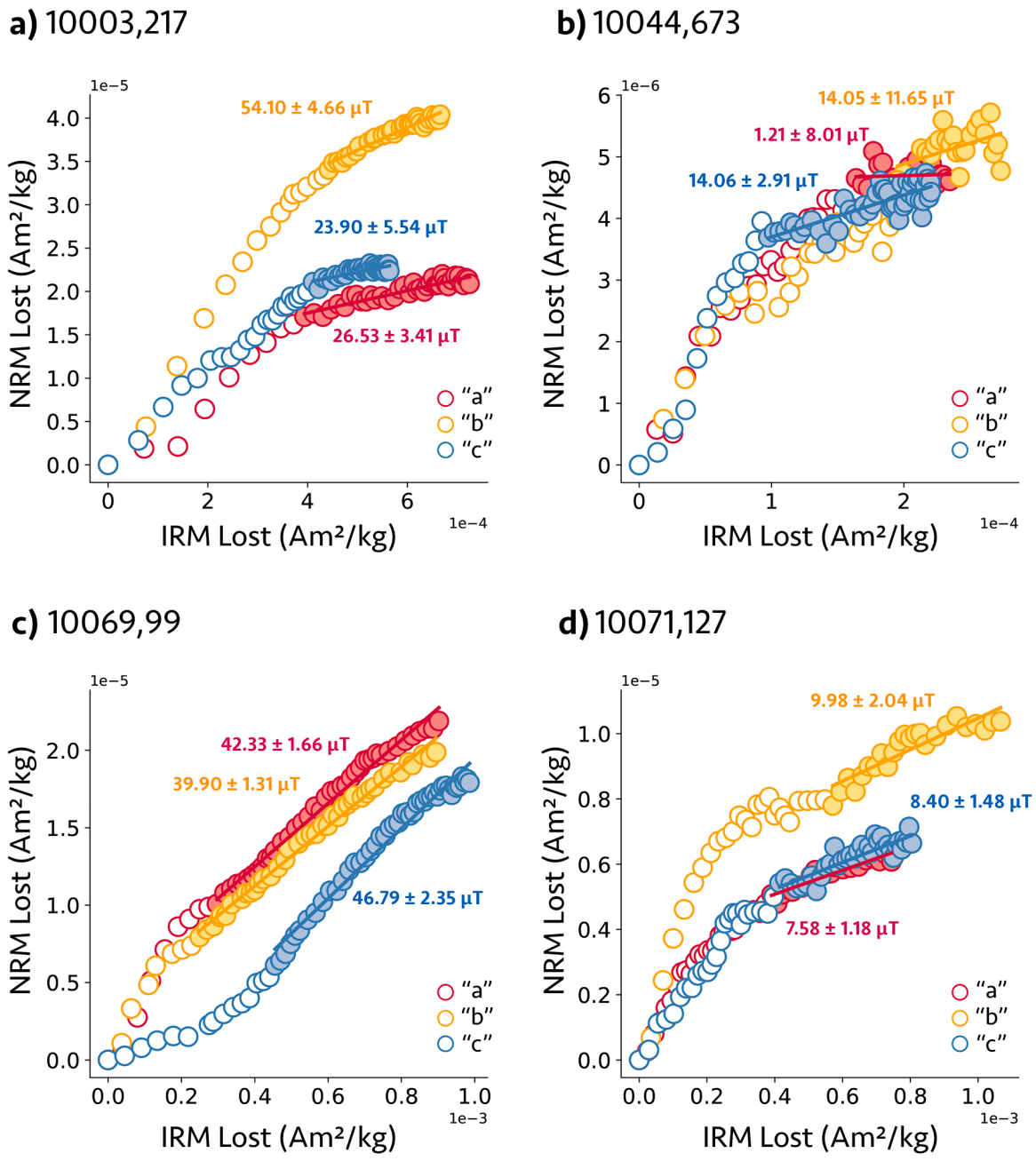

Fig. 5. sIRM paleointensity results. sIRM lost vs NRM lost for (a) 10003,217c, (b) 10044,673c, (c) 10069,99c, (d) 10071,127. Red, blue, and yellow circles represent data from subsamples a, b, and c, respectively. Filled circles denote high coercivity data points used for paleointensity estimations.

IRM [Yu, 2010]. NRM may be carried in more isolated MD grains present within our samples.

Fig. 7 presents the estimated ranges of paleointensity and sample ages, derived through the random selection of ages and paleointensity values based on the distributions. The sIRM paleointensity uncertainties result in considerable spreading due to a substantial geometric σ of 2.20. The 95% confidence intervals for sIRM paleointensity for samples 10003, 10069, and 10071 include paleointensities ranging from 10.21 - 284.39 μT, 7.09 - 250.13 μT, and 1.16 - 56.55 μT, respectively. In contrast, the ARM paleointensity method demonstrates relatively smaller spreading, with 95% confidence intervals for ARM paleointensity for samples 10069 and 10071 being 48.28 - 128.94 μT and 7.06 - 27.72 μT, respectively. In our permutation-based hypothesis testing, our null hypothesis was that "There is no significant difference in the paleointensities between the samples 10069,99 and 10071,127". We employed this test on both ARM and sIRM paleointensity values. The ARM p-value was less than 0.05, indicating a statistical difference between the two data sets and suggesting potential variations in field intensity. Conversely, the sIRM analysis produced a p-value of 0.2814, due to the large uncertainties tied to the sIRM calibration constant 'a' [Shea et al., 2012; Suavet et al., 2013; Nichols et al., 2021] yields similar results to 10069,99. Our results imply that HFE paleointensities may have varied (maximum/minimum) by at least a factor of ~3-11. For context, Earth produced a factor of ~15-19 over the last 400 Myrs [Selkin and Tauxe, 2000; Biggin and Paterson, 2014].

4. Lunar Paleointensity Reliability

The reliability of lunar paleomagnetism measurements has long been questioned, not only due to difficulties in explaining the lunar dynamo

Table 2
Non-heating based paleointensity values, fidelity limit test results, simulated paleointensity estimations by PRM/ magnetic contamination, and estimates of possible VRM contribution.

ID	ARM PI (μT) (AF levels)	sIRM PI (μT) (AF levels)	PFL (μT)	PRM PI (μT)	IRM PI (μT)	VRM (%)	Paleointensity (μT)/field source
10003, 217	14.62 ± 9.29 (24-100 mT)	54.10 ± 4.66* (15-100 mT)	Passed <46.15*	x	3.98 ± 13.09	< 2.10	54.10 ± 4.66 TRM origin
10044, 673	12.24 ± 7.13 (13-100 mT)	9.73 ± 18.42 (13-100 mT)	Failed 23.07	shocked > 5GPa	23.07 ± 25.52	< 1.75	11.01 ± 1.75 Poor recording, SRM
10069, 99	79.91 ± 12.69 (15-100 mT)	43.00 ± 8.68 (8-100 mT)	Passed <7.69	0.50 ± 5.76	6.32 ± 7.33	< 4.28	61.36 ± 26.24 TRM origin
10071, 127	12.72 ± 2.88 (30-100 mT)	8.65 ± 3.03 (30-100 mT)	Passed 7.69	-0.07 ± 6.52	0.89 ± 4.72	< 12.80	10.69 ± 2.87 TRM orgin

The first column contains the Apollo sample ID. The second and third columns contain averaged ARM and sIRM paleointensity values with 95% confidence uncertainties derived from a two-tailed student's t-test (Section 3.1.2).*One subsample 10003,217b only passed PFL test, and we included that for the ultimate paleointensity. The fourth column contains paleointensity fidelity limits (PFL) obtained from our samples (Section 4.2). The fifth column and sixth columns contain simulated paleointensity estimates obtained from the high coercivity fractions within samples that were initially demagnetized and then imparted with either laboratory PRM or laboratory 5 mT IRM (Section 4.2). The seventh column contains the estimated percentage of VRM in our samples relative to their initial NRM intensities. The eighth column contains our overall mean (combining ARM and IRM) paleointensity values for each sample and indicates our interpretation of the initial magnetizing field source.

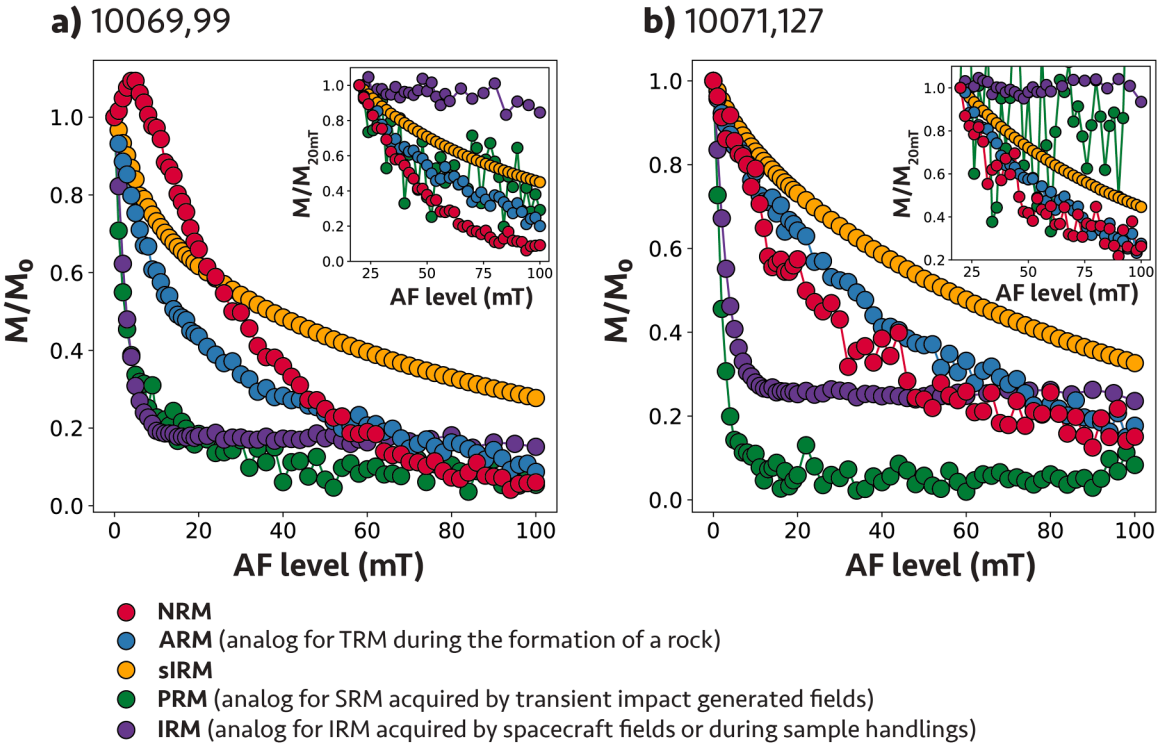

Fig. 6. AF demagnetization curves for samples 10069,99 and 10071,127, featuring normalized natural remanent magnetization (NRM) (red circles), anhysteretic remanent magnetization (ARM) (blue circles), saturated isothermal remanent magnetization (sIRM) (yellow circles), pressure remanent magnetization (PRM) (green circles) for subsample "c", and long-term isothermal remanent magnetization (purple circles) for subsample "b" from each rock. Insets display magnetization normalized at 20 mT. ARMs were acquired with a DC field of 100 μT and an AC field of 200 mT, while sIRMs were acquired in a field of 900 mT. PRMs were obtained by applying ~2 GPa in a DC field of 500 μT during hydrostatic pressure experiments. Long-term IRMs were acquired through a 48-hour exposure to a 5 mT magnetic field produced by a Nd magnet.

power source but also due to the poor rock magnetic properties of lunar materials [Tikoo et al., 2012] and the potential acquisition of secondary magnetic contamination [Lawrence et al., 2008; Tarduno et al., 2021; Weiss and Tikoo, 2014]. To assess the reliability of our paleointensity estimates, while considering possible sources of magnetic contamination, we performed a series of paleomagnetic and rock magnetic experiments, including paleointensity fidelity limit tests [Tikoo et al., 2012], hydrostatic pressure experiments [Gattacceca et al., 2010b], IRM acquisition tests, and VRM acquisition tests [Tikoo and Jung, 2023; Shea et al., 2012].

4.1. Methods

Paleointensity Fidelity Limit Tests: We conducted fidelity limit tests to identify samples with poor magnetic recording properties. Some lunar rocks dominated by MD kamacite may not be capable of accurately recording weak paleofields, or they may exhibit non-linear relationships between TRM and either sIRM or ARM for weak magnetic fields [Ciswoski et al., 1983; Tikoo et al., 2012]. The fidelity limit test involves applying laboratory ARM using different bias fields ranging from ~10 - 100 μT (TRM equivalent field of 7.7 - 76.9 μT), and then using the ARM paleointensity method to retrieve the intensity of the laboratory bias

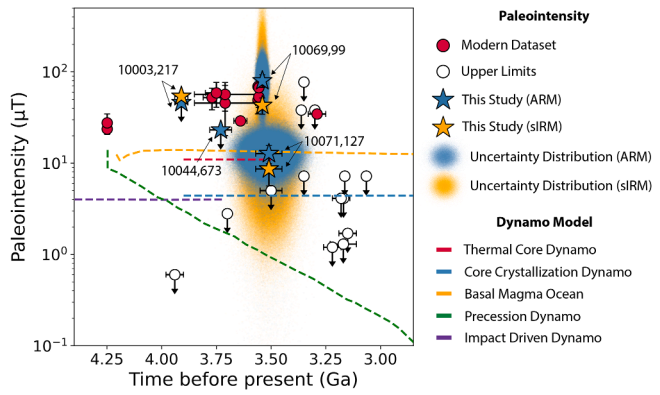

Fig. 7. Paleointensity determinations (μT) vs. radiometric age (Ga) during the HFE period in logarithmic scale. Paleointensity estimates from our study are represented by blue stars (ARM paleointensity) and yellow stars (sIRM paleointensity). Uncertainties are shown as error bars, while upper limits are symbolized as downward arrows. Blue and yellow shadings represent additional paleointensity uncertainties for samples 10069 and 10071 generated by random sampling from distributions associated with uncertainties in sample ages and paleointensity calibration factors. As in Fig. 1, recent studies' paleointensity estimates are shown using red circles, while upper limit values are shown with white circles. Red, blue, yellow, green, and purple dashed lines correspond to the estimated surface field values produced by dynamos powered by thermal core convection [Evans et al., 2018], core crystallization [Evans et al., 2018], basal magma ocean [Scheinberg et al., 2018], precession dynamo [Dwyer et al., 2011], and impacts [Le Bars et al., 2011], respectively.

field and determining the minimum bias field that can be accurately retrieved using AF-based methods (such as the ARM method) in our experiments [method details described in Section S5.1].

Testing for transient impact-generated fields: It has been proposed the magnetization observed in Apollo samples could be shock remanent magnetization (SRM) acquired via transient fields generated by charge separation during impact events [Tarduno et al., 2021; Crawford, 2020]. To quantify possible SRM acquisition, we conducted hydrostatic pressure remanent magnetization (PRM) acquisition experiments on 10069 and 10071 following the methods of [Gattacceca et al., 2010b; Tikoo et al., 2015]. These two samples were chosen because they have stable NRM decay, and they did not show microscopic features of shock $>$ 5 GPa. During PRM experiments, we applied a 500 μT dc field (comparable to estimated impact fields generated from West Crater, the largest nearby crater based on [Crawford, 2020]). Specimens were pressurized and subsequently decompressed from peak pressures up to 2 GPa in the presence of the applied field [method details described in Section S5.2]. The demagnetization behavior of PRM was then compared to that of the NRM in our samples.

Testing for IRM acquisition by spacecraft fields and sample handling: It also has been proposed that lunar rocks may become remagnetized by exposure to ~2-5 mT fields generated from the spacecraft electronics during sample transit or during sample preparation using magnetic tools [Strangway et al., 1973; Lawrence et al., 2008]. To evaluate the effect of IRM contamination on lunar rocks, recent studies applied long-term (5 mT) and instantaneously acquired (10 mT) IRM to various lunar rock samples. The resulting magnetic contamination could be removed from most samples by AF levels of ~10-40 mT [Tikoo and Jung, 2023; Cai et al., 2022]. We conducted both long-term and instantaneous IRM acquisition experiments for our subsamples following the method of Tikoo and Jung [2023]. For the long-term IRM experiment, we exposed each previously AF demagnetized "b" subsample to a 5mT field (generated using an Nd magnet) for 48 hours [Refer to Fig. S1 in Tikoo and Jung, 2023 for details on the experimental setup]. For the instantaneous test, we applied a 10 mT IRM to each "a" subsample on top of a previously imparted 100 μT bias field ARM (analogous to samples bearing TRM before exposure to IRM) [method details described in Section S5.3]. The demagnetization behaviors of samples following these two complementary tests were also compared to those of the NRM in our lunar rocks. In addition, we calculated HC paleointensity estimates after exposing samples to IRM during both experiments to assess whether this IRM overprint affects HC components or if it can be removed at LC through AF demagnetization.

Testing for VRM acquired from Earth's magnetic field: Previous studies indicate that VRM acquisition from the geomagnetic field after sample delivery to the Earth cannot be the origin of the entire NRM observed within numerous lunar mare basalts [Shea et al., 2012; Suavet et al., 2013; Strauss et al., 2021]. Nevertheless, we conducted a series of VRM acquisition tests on our samples to estimate the amount of VRM gained during 52 years of exposure to Earth's magnetic field (approximately 50 μT). We imparted samples with a one-week-long VRM by placing both un-demagnetized (pristine) and previously AF demagnetized specimens (up to 100 mT) outside of the magnetically shielded room and compared the amount of VRM gained to our NRM intensities [method details described in Section S5.4].

4.2. Results

Paleointensity Fidelity Limit Tests: We found that the lowest retrievable paleointensity values for samples 10003,217 and 10044,673 are ~46 μT and ~23 μT, respectively. These values are higher than their ARM paleointensity estimations for their NRMs' HC remanence components, calling into question the fidelity of the obtained paleointensity values. As such, we only included the paleointensity measured for subsample 10003,217b via the sIRM method as a valid value for this sample. Paleointensity fidelity limits for samples 10069,99 and 10071,127 were $<$8 μT. HC component paleointensities from these two samples exceeded this threshold (for both ARM and sIRM paleointensity determinations), indicating the retrieved paleointensities are reliable.

Testing for transient impact-generated fields: AF demagnetization of 2 GPa PRMs acquired during our pressure experiments on 10069 and 10071 behaved very differently from those of NRM for these samples. In both cases, the laboratory PRM appears to be fully removed $<$ AF 40 mT [Fig. 7]. Since HC fractions were considered for our paleointensity estimation, the contribution of the transient impact-generated fields to the preserved magnetization would be minimal. We calculated paleointensities for the HC fraction of our laboratory PRMs and obtained values of 0.50 ± 5.76 μT for sample 10069 and -0.07 ± 76.52 μT for sample 10071, thereby demonstrating that PRM cannot account for the $>$10 μT HC component paleointensities observed in these rocks. Broadly, PRM experiments on lunar materials indicate that the AF level required to fully demagnetize PRM does not typically exceed 40-50 mT, irrespective of pressure level (2 GPa - 10 GPa), duration of pressure exposure (10^{-9} - 10^{1}s), applied field, and the number of impact events [Gattacceca et al., 2007; 2010b; Tikoo et al., 2015]. Additionally, we note that the absence of HC magnetization within shocked sample 10044 provides further evidence that our samples do not record SRM from transient impact fields.

Testing for IRM acquisition by spacecraft fields and sample handling: Our long-term (48-hour) laboratory IRM was mostly demagnetized by AF levels $<$20 mT for all of our samples [Fig. 7]. Fitting paleointensities to the HC fraction (AF $>$20 mT) of our laboratory IRMs for samples 10003, 10044, 10069, and 10071 yielded values of 3.98 ± 13.09 μT, 23.07 ± 25.52 μT, 6.32 ± 7.38 μT, and 0.89 ± 4.72 μT, respectively. These retrieved paleointensity values are all within error of zero, indicating that magnetic contamination generally cannot account for the HC NRM in our samples (particularly 10003, 10069 and 10071). The instantaneous IRM experiment yielded paleointensity values that were close to the expected 100 μT (range of 83 to 117 μT) ARM for all samples.

Testing for VRM acquired from Earth's magnetic field: Our VRM experiments revealed that both un-demagnetized and fully demagnetized specimens from our mare basalts would have acquired$<$15% of their total NRM as VRM from the geomagnetic field during their

residence time on Earth. Moreover, VRM is typically acquired by low-coercivity multi-domain grains, and the VRM components can be easily removed through AF cleaning at low coercivities [Acton et al., 2007; Gattacceca and Rochette, 2004]. These factors collectively indicate that VRM cannot explain the HC NRM in our samples.

5. Discussion

Our results reveal that diverse magnetization histories are recorded in HFE-aged Apollo 11 mare basalt samples. One previously unstudied sample, 10071, yielded a paleointensity value of 10.69 ± 2.87 μT, which is approximately an order of magnitude lower than many recent paleointensity estimates for HFE mare basalts [Cournède et al., 2012; Shea et al., 2012; Suavet et al., 2013; Weiss and Tikoo, 2014; Nichols et al., 2021]. However, our results for sample 10003 and 10069 differ somewhat from previous paleomagnetic studies of the same rocks. We obtained a 54.10 ± 4.66 μT and 61.36 ± 26.24 μT paleointensity value for 10003,217b and 10069,99. In contrast, Apollo-era studies reported these samples to have far lower paleointensities. Sample 10003 was previously reported to have a paleointensity of ~4 μT (determined using the non-heating-based REMc method) [Ciscowski et al., 1983]. For sample 10069, a 1.51 μT paleointensity value was obtained via the Thellier-Thellier double heating method [Helsey, 1970], and a 2.29 μT paleointensity was obtained via the REMc method [Cisowski et al., 1983]. Below, we discuss possible reasons for why our paleointensity values for 10003 and 10069 differed from the previous works:

First, the Thellier-Thellier paleointensity experiment described in Helsey [1970] involved heating the sample in air rather than in a controlled oxygen fugacity environment. Lunar mare basalts formed in reducing conditions (approximately 1 log unit below the iron-wüstite buffer [Sato et al., 1973]). Therefore, it is likely that sample 10069 experienced significant thermochemical alteration during the Apollo-era study, making it difficult to retrieve an accurate paleointensity [Suavet et al., 2014]. Second, the REMc method used by Ciswoski et al., [1983] relied on normalizing NRM by sIRM at a single demagnetization step (AF 20 mT), which may not accurately represent the HC magnetization component of the sample. It is also possible that the subsample of 10003 and 10069 studied by Ciswoski et al., [1983] had a poorer magnetic recording fidelity than our subsample and that an accurate paleointensity could not be retrieved by that work. For example, Tikoo et al. [2014] determined that the paleointensity fidelity limit for mare basalt 15556 was ~75 μT, even higher than the paleointensity we obtained for 10003,217 and 10069,99. Other studies have demonstrated that heterogeneity within basalt samples can lead to different subsamples having different paleointensity fidelity limits [Nichols et al., 2021].

10003,217b, 10069,99 and 10071,127 contain stable HC remanence components with associated paleointensities that exceed their fidelity limit threshold values. Our pressure experiments indicate that SRM acquired from transient impact plasma fields would be confined to low coercivity magnetic grains and cannot readily explain the observed HC magnetization in sample 10069,99 and 10071,127. We again note that our one visibly shocked sample 10044,673 did not contain any stable HC remanence, further suggesting that lunar basalts do not retain records of impact fields [Gattacceca et al, 2010a; Tikoo et al., 2015]. Since the magnitude of shock remagnetization increases with pressure, it is possible that the higher shock pressures experienced by sample 10044 demagnetized it through a higher coercivity range than the other less shocked samples in this study [Gattacceca et al, 2007; Louzada et al., 2010].

Our long-term and instantaneous IRM acquisition experiments as well as our VRM experiments collectively imply that HC magnetization components in 10003, 10069 and 10071 are unlikely to be produced by magnetic contamination from tools, spacecraft fields, or Earth's magnetic field. We further note that none of our samples were obtained from near-circular saw or band saw cut faces of the parent Apollo samples, thus precluding saw-cutting-related remagnetization (discussed for other lunar samples in Tikoo et al. [2014] and Mighani et al. [2020]) as an origin of HC remanence in our samples as well. These results are consistent with the outcomes of other studies that explored the possibility of magnetic contamination in lunar basalt samples [Cai et al., 2022; Tikoo and Jung, 2023; Cournède et al., 2012; Shea et al., 2012; Suavet et al., 2013; Weiss and Tikoo, 2014; Nichols et al., 2021; Tikoo et al., 2012; 2014].

Numerous recent lunar paleomagnetism studies focusing on mare basalts recovered strong (>~40 μT) lunar paleofields during the HFE [Cournède et al., 2012; Shea et al., 2012; Suavet et al., 2013; Weiss and Tikoo, 2014; Nichols et al., 2021]. However, some recent papers also reported possibly low or null paleointensity. Two breccias (62235 and 72215), formed between approximately 3.8-3.9 Ga, indicated paleointensities < 3μT for high temperature components [Lawrence et al., 2008]. Three mare basalts, aged approximately 3.7-3.85 Ga, analyzed by Cournède et al. [2012] using the sIRM method did not contain recoverable dynamo records, which may suggest they were likely magnetized in weak or null fields < 11 μT. Tarduno et al. [2021] reported null paleointensity values for small mm-scale fragments from two HFE-aged samples (feldspathic basalt 14053 and ilmenite basalt 71055).

It is unclear whether the discrepant results between these studies and other modern lunar paleomagnetism studies reflect true lunar paleointensity variability or whether they can be explained by methodological issues associated with contrasting paleointensity methods. For example, considering the complex history of breccia samples, the paleointensity measured by Lawrence et al., 2008 might have been affected by multiple shock and recrystallization events. In the case of Cournède et al. [2012], the observed results could be a result of poor magnetic recording properties rather than the evidence of inherently low paleointensity values. While most mare basalt paleomagnetism studies have used room-temperature paleointensity methods to avoid thermochemically altering samples, the Tarduno et al. [2021] study used a CO_2 laser to heat samples in air to temperatures of 590 °C (90-180 s per heating step) and estimated paleointensities based on the ratio of NRM remaining after zero-field heating to 590 °C and the magnitude of partial TRM gained after in-field heating to 590 °C. We note that even short-period laser heating can thermochemically alter troilite (an antiferromagnetic mineral that often co-occurs in eutectic assemblages with ferromagnetic kamacite in mare basalts) to form magnetite [Li et al., 2023]. Such alteration could potentially result in inaccurate paleointensity determinations if robust checks for thermochemical alteration are not utilized. Creation of new magnetic carriers or decomposition of MD carriers to SD grains may increase pTRM during the experiment, leading to paleointensity underestimation.

In summary, despite the uncertainties associated with our paleointensity methods, our results generally support the hypothesis that the Moon may have experienced substantial paleofield variability during the HFE period. This variability in paleointensity could reflect long-term field behavior such as magnetic reversals, excursions, or secular variation [Selkin and Tauxe, 2000]. Alternatively, lunar paleointensity variability may indicate that a dynamo mechanism capable of producing intense fields might have operated intermittently instead of continuously during the lunar HFE [Evans et al., 2018; Evans and Tikoo, 2022]. This is because lunar thermal evolution models reveal that maintaining a convective-driven lunar dynamo capable of generating fields >10 μT throughout the HFE is challenging [Evans et al., 2018]. In conclusion, lunar crustal magnetism and paleomagnetism studies suggest that the Moon generated a long-lived dynamo [Weiss et al., 2023]. Our work corroborates these previous findings and further demonstrates that magnetic field intensity variability may have occurred on the ancient Moon at a magnitude roughly comparable to how Earth's field has varied for the past 400 Myr.

Open Research

Paleomagnetic data from this study are available on the Magnetics Information Consortium (MagIC) database https://www2earthref.org/MagIC/19922 at doi: 10.7288/V4/MAGIC/19922, https://earthref.org/MagIC/19922/d409c9e3-62eb-4f59-b10b-cd611b3ba80a. SEM and TEM images, FORCs, and hysteresis data acquired as a part of this study are available on Zenodo, a permanent CERN-backed online data repository, at doi: 10.5281/zenodo.11100248.

CRediT authorship contribution statement

Ji-In Jung: Writing – review & editing, Writing – original draft, Methodology, Investigation, Funding acquisition, Formal analysis, Data curation, Conceptualization. **Sonia M. Tikoo:** Writing – review & editing, Writing – original draft, Supervision, Resources, Project administration, Methodology, Investigation, Funding acquisition. **Dale Burns:** Writing – review & editing, Resources, Methodology, Investigation. **Zoltán Váci:** Writing – review & editing, Methodology, Investigation. **Michael J. Krawczynski:** Writing – review & editing, Methodology, Investigation, Funding acquisition.

Declaration of competing interest

The authors declare that they have no known competing financial interests or personal relationships that could have appeared to influence the work reported in this paper.

Data availability

Paleomagnetic data will be made public in MagIC database upon publication. We provide a link to review copy in the ms. All other data is on zenodo (doi in ms).

Acknowledgments

We thank R. Ziegler and J. Gross, CAPTEM, and the Lunar Receiving Laboratory at Johnson Space Center for allocating and preparing our samples. We thank B. Weiss and E. Lima for allowing us to conduct ARM paleointensity, fidelity limit tests, and hydrostatic pressure experiments at the Massachusetts Institute of Technology (MIT) paleomagnetism laboratory. We also thank the Institute of Rock Magnetism (IRM) at the University of Minnesota, especially P. Solheid, for assistance with hysteresis and FORC measurements. We thank Huafang Li for helping with TEM experiments at Washington University in Saint Louis. We are grateful to J. Gattacceca and C. Nichols for helpful reviews, and J. Badro for editorial handling. This research was supported by NASA award numbers 80NSSC21K1541, 80NSSC20K0640, and 80NSSC23M0161, as well as a Stanford Doerr School of Sustainability Discovery Grant.

Supplementary materials

Supplementary material associated with this article can be found, in the online version, at doi:10.1016/j.epsl.2024.118757.

References

Acton, G., Yin, Z., Verosub, K.L., Jovane, L., Roth, A., Jacobsen, B., Ebel, D.S., 2007. Micromagnetic coercivity distributions and interactions in chondrules with implications for paleointensities of the early solar system. J. Geophys. Res.: Solid Earth 112 (B3). https://doi.org/10.1029/2006JB004655.

Beaty, D.W., Albee, A.L., 1980. The geology and petrology of the Apollo 11 landing site. Lunar Planetary Sci. Conf. Proc. 1, 23–35.

Biggin, A.J., Paterson, G.A., 2014. A new set of qualitative reliability criteria to aid inferences on palaeomagnetic dipole moment variations through geological time. Front. Earth. Sci. (Lausanne) 2, 113524. https://doi.org/10.3389/feart.2014.00024.

Cai, S., Qin, H., Deng, C., Liu, S., Chen, Y., He, H., Pan, Y., 2022. Magnetic property and paleointensity study of the lunar regolith (E21). Acta Petrologica Sinica 38 (6), 1832–1842. https://doi.org/10.18654/1000-0569/2022.06.20.

Cébron, D., Laguerre, R., Noir, J., Schaeffer, N., 2019. Precessing spherical shells: Flows, dissipation, dynamo and the lunar core. Geophys. J. Int. 219, S34–S57. https://doi.org/10.1093/gji/ggz037.

Cisowski, S.M., Collinson, D.W., Runcorn, S.K., Stephenson, A., Fuller, M., 1983. A review of lunar paleointensity data and implications for the origin of lunar magnetism. J. Geophys. Res.: Solid Earth 88, A691–A704. https://doi.org/10.1029/JB088iS02p0A691.

Cournède, C., Gattacceca, J., Rochette, P., 2012. Magnetic study of large apollo samples: Possible evidence for an ancient centered dipolar field on the moon. Earth. Planet. Sci. Lett. 331-332, 31–42. https://doi.org/10.1016/j.epsl.2012.03.004.

Crawford, D.A., 2020. Simulations of magnetic fields produced by asteroid impact: Possible implications for planetary paleomagnetism. Int. J. Impact. Eng. 137, 103464 https://doi.org/10.1016/j.ijimpeng.2019.103464.

Dunlop, D.J., 1973. Theory of the magnetic viscosity of lunar and terrestrial rocks. Rev. Geophys. 11 (4), 855–901. https://doi.org/10.1029/RG011i004p00855.

Dwyer, C.A., Stevenson, D.J., Nimmo, F., 2011. A long-lived lunar dynamo driven by continuous mechanical stirring. Nature 479 (7372), 212–214. https://doi.org/10.1038/nature10564.

Evans, A.J., Tikoo, S.M., 2022. An episodic high-intensity lunar core dynamo. Nat. Astron. 6 (3), 325–330. https://doi.org/10.1038/s41550-021-01574-y.

Evans, A.J., Tikoo, S.M., Andrews-Hanna, J., 2018. The case against an early lunar dynamo powered by core convection. Geophys. Res. Lett. 45 (1), 98–107. https://doi.org/10.1002/2017GL075441.

Fritz, J.ö, Greshake, A., Fernandes, V.A., 2017. Revising the shock classification of meteorites. Meteorit. Planet. Sci. 52 (6), 1216–1232. https://doi.org/10.1111/maps.12845.

Fuller, M., Cisowski, S.M., 1987. Lunar paleomagnetism. Springer US, Boston, MA, pp. 668–673. Geophysics.

Garrick-Bethell, I., Weiss, B.P., Shuster, D.L., Tikoo, S.M., Tremblay, M.M., 2017. Further evidence for early lunar magnetism from troctolite 76535. J. Geophys. Res.: Planets 122 (1), 76–93. https://doi.org/10.1002/2016JE005154.

Garrick-Bethell, I., Weiss, B.P., Shuster, D.L., Buz, J., 2009. Early lunar magnetism. Science (1979) 323, 356–359. https://doi.org/10.1126/science.1166804.

Gattacceca, J., Boustie, M., Lima, E., Weiss, B., De Resseguier, T., Cuq-Lelandais, J., 2010a. Unraveling the simultaneous shock magnetization and demagnetization of rocks. Phys. Earth Planetary Interiors 182 (1-2), 42–49. https://doi.org/10.1016/j.pepi.2010.06.009.

Gattacceca, J., Boustie, M., Hood, L., Cuq-Lelandais, J., Fuller, M., Bezaeva, N.S., 2010b. Can the lunar crust be magnetized by shock: Experimental groundtruth. Earth. Planet. Sci. Lett. 299 (1), 42–53. https://doi.org/10.1016/j.epsl.2010.08.011.

Gattacceca, J., Lamali, A., Rochette, P., Boustie, M., Berthe, L., 2007. The effects of explosive-driven shocks on the natural remanent magnetization and the magnetic properties of rocks. Physics Earth Planetary Interiors 162 (1), 85–98. https://doi.org/10.1016/j.pepi.2007.03.006.

Gattacceca, J., Rochette, P., 2004. Toward a robust normalized magnetic paleointensity method applied to meteorites. Earth. Planet. Sci. Lett. 227 (3-4), 377–393. https://doi.org/10.1016/j.epsl.2004.09.013.

Guggisberg, S., Eberhardt, P., Geiss, J., Grogler, N., Stettler, A., Brown, G.M., Pecket, A., 1979. Classification of the Apollo-11 basalts according to Ar39-Ar40 ages and petrological properties. In: Proceeding 10th Lunar Planetary Science Conference, pp. 1–39.

Halekas, J.S., Lin, R.P., Mitchell, D.L., 2003. Magnetic fields of lunar multi-ring impact basins. Meteorit. Planet. Sci. 38 (4), 565–578. https://doi.org/10.1111/j.1945-5100.2003.tb00027.x.

Hamid, S.S., O'Rourke, J.G., Soderlund, K.M., 2023. A long-lived lunar magnetic field powered by convection in the core and a basal magma ocean. Planet. Sci. J. (4), 88. https://doi.org/10.3847/PSJ/accb99.

Harrison, R.J., Feinberg, J.M., 2008. FORCinel: An improved algorithm for calculating first-order reversal curve distributions using locally weighted regression smoothing. Geochem., Geophys., Geosyst. 9 (5) https://doi.org/10.1029/2008GC001987.

Helsley, C.E., 1970. Magnetic properties of lunar 10022, 10069, 10084 and 10085 samples. Geochimica Et Cosmochimica Acta Supplement 1, 2213.

Hood, L.L., 2011. Central magnetic anomalies of Nectarian-aged lunar impact basins: Probable evidence for an early core dynamo. Icarus 211 (2), 1109–1128. https://doi.org/10.1016/j.icarus.2010.08.012.

Hood, L.L., Torres, C.B., Oliveira, J.S., Wieczorek, M.A., Stewart, S.T., 2021. A new large-scale map of the lunar crustal magnetic field and its interpretation. J. Geophys. Res.: Planets 126 (2). https://doi.org/10.1029/2020JE006667 e2020JE006667.

Hood, L.L., Spudis, P.D., 2016. Magnetic anomalies in the Imbrium and Schrödinger impact basins: Orbital evidence for persistence of the lunar core dynamo into the Imbrian epoch. J. Geophys. Res.: Planets 121 (11), 2268–2281. https://doi.org/10.1002/2016JE005166.

Kirschvink, J.L., 1980. The least-squares line and plane and the analysis of palaeomagnetic data. Geophys. J. Int. 62 (3), 699–718. https://doi.org/10.1111/j.1365-246X.1980.tb02601.x.

Lawrence, K., Johnson, C., Tauxe, L., Gee, J., 2008. Lunar paleointensity measurements: Implications for lunar magnetic evolution. Phys. Earth Planetary Interiors 168 (1), 71–87. https://doi.org/10.1016/j.pepi.2008.05.007.

Le Bars, M., Wieczorek, M.A., Karatekin, Ö, Cébron, D., Laneuville, M, 2011. An impact-driven dynamo for the early moon. Nature 479 (7372), 215–218. https://doi.org/10.1038/nature10565.

Lepaulard, C., Gattacceca, J., Uehara, M., Rochette, P., Quesnel, Y., Macke, R.J., Kiefer, S.W., 2019. A survey of the natural remanent magnetization and magnetic

susceptibility of Apollo whole rocks. Phys. Earth Planetary Interiors 290, 36–43. https://doi.org/10.1016/j.pepi.2019.03.004.
Li, X., Chen, Y., Tang, X., Gu, L., Yuan, J., Su, W., Tian, H., Luo, H., Cai, S., Komarneni, S., 2023. Thermally induced phase transition of troilite during micro-raman spectroscopy analysis. Icarus 390, 115299. https://doi.org/10.1016/j.icarus.2022.115299.
Louzada, K.L., Stewart, S.T., Weiss, B.P., Gattacceca, J., Bezaeva, N.S., 2010. Shock and static pressure demagnetization of pyrrhotite and implications for the Martian crust. Earth. Planet. Sci. Lett. 290 (1-2), 90–101. https://doi.org/10.1016/j.epsl.2009.12.006.
Luo, Y., Chen, H., Beard, S., Zeng, X., Hu, S., Du, Z., Jin, L., Liu, J., Li, S., Zhang, X., 2024. EBSD Analysis of iron-nickel metal in l type ordinary chondrites: 1. The microstructural shock signatures. J. Geophys. Res.: Planets 129 (1). https://doi.org/10.1029/2023JE007938 e2023JE007938.
Maxbauer, D.P., Feinberg, J.M., Fox, D.L., 2016. MAX UnMix: A web application for unmixing magnetic coercivity distributions. Comput. Geosci. 95, 140–145. https://doi.org/10.1016/j.cageo.2016.07.009.
Mighani, S., Wang, H., Shuster, D.L., Borlina, C.S., O Nichols, C.I., Weiss, B.P, 2020. The end of the lunar dynamo. Sci. Adv. aax0883.
Muxworthy, A.R., Williams, W., 2015. Critical single-domain grain sizes in elongated iron particles: Implications for meteoritic and lunar magnetism. Geophys. J. Int. 202 (1), 578–583.
Nichols, C.I.O., Weiss, B.P., Getzin, B.L., Schmitt, H.H., Béguin, A., Rae, A.S.P., 2021. The palaeoinclination of the ancient lunar magnetic field from an apollo 17 basalt. Nat. Astron. 5 (12), 1216–1223. https://doi.org/10.1038/s41550-021-01469-y.
Ohtani, E., Sakurabayashi, T., Kurosawa, K., 2022. Experimental simulations of shock textures in BCC iron: Implications for iron meteorites. Prog. Earth. Planet. Sci. 9 (1), 1–15. https://doi.org/10.1186/s40645-022-00482-7.
Oliveira, J.S., Wieczorek, M.A., Kletetschka, G., 2017. Iron abundances in lunar impact basin melt sheets from orbital magnetic field data. J. Geophys. Res: Planets 122 (12), 2429–2444. https://doi.org/10.1002/2017JE005397.
Robertson, D.J., France, D.E., 1994. Discrimination of remanence-carrying minerals in mixtures, using isothermal remanent magnetisation acquisition curves. Phys. Earth Planetary Interiors 82 (3), 223–234. https://doi.org/10.1016/0031-9201(94)90074-4.
Sato, M., Tuthill Helz, R., Hickling, N, 1973. Oxygen fugacity values of some lunar rocks. Lunar Planetary Sci. Conf. Proc. 4, 650.
Scheinberg, A.L., Soderlund, K.M., Elkins-Tanton, L.T., 2018. A basal magma ocean dynamo to explain the early lunar magnetic field. Earth. Planet. Sci. Lett. 492, 144–151. https://doi.org/10.1016/j.epsl.2018.04.015.
Selkin, P.A., Tauxe, L., 2000. Long-term variations in palaeointensity. Philos. Trans. Royal Soc. London. Series A: Math., Phys. Eng. Sci. 358 (1768), 1065–1088. https://doi.org/10.1098/rsta.2000.0574.
Shea, E.K., Weiss, B.P., Cassata, W.S., Shuster, D.L., Tikoo, S.M., Gattacceca, J., 2012. A long-lived lunar core dynamo. Science (1979) 335 (6067), 453–456. https://doi.org/10.1126/science.1215359.
Stephenson, A., 1980. A gyroremanent magnetisation in anisotropic magnetic material. Nature 284 (5751), 49–51. https://doi.org/10.1038/284049a0.
Stettler, A., Eberhardt, P., Geiss, J., Groegler, N., Maurer, P., 1974. On the duration of lava flow activity in mare tranquilitatis. Lunar Planetary Sci. Conf. Proc. 2, 1557–1570.
Strangway, D.W., Gose, W.A., Pearce, G.W., Carnes, J.G., 1973. Magnetism and the history of the Moon. Am. Inst. Phys. Conf. Proc. 10 (1), 1178–1196, 1.
Strauss, B.E., Tikoo, S.M., Gross, J., Setera, J.B., Turrin, B., 2021. Constraining the Decline of the lunar dynamo field at ≈3.1 Ga through paleomagnetic analyses of apollo 12 mare basalts. J. Geophys. Res.: Planets 126 (3). https://doi.org/10.1029/2020JE006715 e2020JE006715.
Stöffler, D., Hamann, C., Metzler, K., 2018. Shock metamorphism of planetary silicate rocks and sediments: Proposal for an updated classification system. Meteoritics Planetary Sci. 53, 5–49. https://doi.org/10.1111/maps.12912.
Stöffler, D., Ryder, G., Ivanov, B.A., Artemieva, N.A., Cintala, M.J., Grieve, R.A.F., 2006. Cratering history and lunar chronology. Rev. Mineral. Geochem. 60 (1), 519–596. https://doi.org/10.2138/rmg.2006.60.05.
Suavet, C., Weiss, B.P., Grove, T.L., 2014. Controlled-atmosphere thermal demagnetization and paleointensity analyses of extraterrestrial rocks. Geochem., Geophys., Geosyst. 15 (7), 2733–2743. https://doi.org/10.1002/2013GC005215.
Suavet, C., Weiss, B.P., Cassata, W.S., Shuster, D.L., Gattacceca, J., Chan, L., 2013. Persistence and origin of the lunar core dynamo. Proc. National Acad. Sci. 110 (21), 8453–8458. https://doi.org/10.1073/pnas.1300341110.
Sugiura, N., 1979. ARM, TRM and magnetic interactions: Concentration dependence. Earth. Planet. Sci. Lett. 42 (3), 451–455. https://doi.org/10.1016/0012-821X(79)90054-2.
Stys, C., Dumberry, M., 2020. A past lunar dynamo thermally driven by the precession of its inner core. J. Geophys. Res.: Planets 125 (7), e2020JE006396. https://doi.org/10.1029/2020JE006396.
Tarduno, J.A., Cottrell, R.D., Lawrence, K., Bono, R.K., Huang, W., Johnson, C.L., 2021. Absence of a long-lived lunar paleomagnetosphere. Sci. Adv. 7 (32), eabi7647. https://doi.org/10.1126/sciadv.abi7647.
Tikoo, S.M., Gattacceca, J., Swanson-Hysell, N., Weiss, B.P., Suavet, C., Cournède, C., 2015. Preservation and detectability of shock-induced magnetization. J. Geophys. Res.: Planets 120 (9), 1461–1475. https://doi.org/10.1002/2015JE004840.
Tikoo, S.M., Jung, J., 2023. Establishing a Lunar Origin for Paleomagnetic Records in Apollo Samples. Geophys. Res. Lett. 50 (19) https://doi.org/10.1029/2023GL105152 e2023GL105152.
Tikoo, S.M., Weiss, B.P., Cassata, W.S., Shuster, D.L., Gattacceca, J., Lima, E.A., Suavet, C., Nimmo, F., Fuller, M.D., 2014. Decline of the lunar core dynamo. Earth. Planet. Sci. Lett. 404, 89–97. https://doi.org/10.1016/j.epsl.2014.07.010.
Tikoo, S.M., Weiss, B.P., Buz, J., Lima, E.A., Shea, E.K., Melo, G., 2012. Magnetic fidelity of lunar samples and implications for an ancient core dynamo. Earth. Planet. Sci. Lett. 337-338, 93–103. https://doi.org/10.1016/j.epsl.2012.05.024.
Tikoo, S.M., Weiss, B.P., Shuster, D.L., Suavet, C., Wang, H., Grove, T.L., 2017. A two-billion-year history for the lunar dynamo. Sci. Adv. 1700207.
Turner, G., 1970. Argon-40/argon-39 dating of lunar rock samples. Science (1979) 167 (3918), 466–468. https://doi.org/10.1126/science.167.3918.466.
Weiss, B.P., Tikoo, S.M., 2014. The lunar dynamo. Science (1979) 346 (6214), 1246753. https://doi.org/10.1126/science.1246753.
Weiss, B.P., Wiecorek, M.A., Gattacceca, J., Tikoo, S.M., McDonald, C., Hodges, K.V., Lepaulard, C., 2023. Evidence for a long-lived lunar dynamo from magnetization in Apollo samples and the lunar crust. In: 54th Lunar and Planetary Science Conference 2023, p. 1627.
Wieczorek, M.A., Weiss, B.P., Breuer, D., Cébron, D., Fuller, M., Garrick-Bethell, I., 2023. Lunar Magnetism. Rev. Mineral. Geochem. 89 (1), 207–241. https://doi.org/10.2138/rmg.2023.89.05.
Yu, Y., 2010. Paleointensity determination using anhysteretic remanence and saturation isothermal remanence. Geochem. Geophys., Geosyst. 11 (2) https://doi.org/10.1029/2009GC002804.